

Viscous Flow and Performance Issues in a 6:1 Supersonic Mixed-Flow Compressor with a Tandem Diffuser

Aravinth Sadagopan¹ and Cengiz Camci²

Dept. of Aerospace Engineering, The Pennsylvania State University, University Park, PA 16802

The advancement of multi-dimensional and viscous computational tools has eased the accessibility and overall effort for thorough analysis of complex turbomachinery designs. In this paper, we computationally evaluate a high-pressure ratio supersonic mixed-flow compressor stage designed using an in-house mean-line code. Objective is to include three dimensionalities, viscous flow and compressibility effects including the shock wave systems into account. As mixed-flow compressors are advantageous especially for small jet engine applications we choose mass flow rate, stage total pressure ratio and maximum diameter as the main design constraints. This computational analysis is the second paper of a two-part series explaining strategy for designing a high-pressure ratio mixed-flow compressor stage. The high-pressure ratio and small diameter requirements push this compressor for a highly-loaded supersonic ‘shock-in rotor’ design with supersonic stator/diffuser.

The used RANS based computational fluid dynamics model is thoroughly assessed for its ability to predict compressor performance using existing well-established experimental data. NASA Rotor 37 and RWTH Aachen supersonic tandem stator are chosen as the test cases for exhibiting similar flow characteristics to present design. The computational approach helps to shed light upon the mixed-rotor and supersonic-stator 3D shock structures and viscous/secondary flow. Stage performance map, pressure and velocity distribution of this high-pressure ratio mixed-flow compressor is obtained. Areas of design optimization are highlighted to further improve performance and efficiency. The in-house mean-line design code predicted a pressure ratio of 6.0 with 75.5 % efficiency for a mass flow rate of 3.5 kg/s. The mean-line code obviously lacked to fully represent three-dimensionality effects due to its inherent over-simplifying assumptions thus, inclusion of RANS based computations improves the fidelity of mixed-flow compressor design performance calculations at a great rate. Comprehensive computational analysis of the stage shows that our design goal is met with a stage total pressure ratio of $\Pi_{TT}=5.83$ with an efficiency of $\eta_{IS}=77\%$ for a mass flow rate of $\dot{m}=3.03$ kg/s. A total pressure ratio of 6.12 at 75.5 % efficiency is reached with a 3.5 % increase in design rotational speed.

Keywords: Aero-jet engine, gas turbine system, compressor, mixed-flow, compressible fluid flow, shock waves, RANS analysis, diffuser experiment, rotor experiment, performance charts.

¹ Graduate Research Assistant, Dept. of Aerospace Eng., 47B Hammond Bldg., University Park PA 16802.

² Professor of Aerospace Eng., ASME Fellow, Dept. of Aerospace Eng., 223 Hammond Bldg., University Park PA 16802.

Nomenclature

BL	=	Boundary layer
C_P	=	Pressure Coefficient, $[P-P_1] / [P_{o1}-P_1]$
C_s	=	Casing separation
CFD	=	Computational fluid dynamics
CFL	=	Courant Number
DP	=	Design point
HLV	=	Hub Leading-edge vortices
Kn	=	Knudsen number
L	=	Axial length, [m]
L_s	=	Leading edge separation
\dot{m}	=	Mass flow rate [Kg/s]
\dot{m}/\dot{m}_{DP}	=	Normalized mass flow rate
M_{rel}	=	Relative Mach number
M	=	Mach number
OS	=	Oblique shock
P_o	=	Stagnation pressure, [Pa]
P	=	Static Pressure, [Pa]
P_s	=	Passage Shock
PS	=	Pressure side
r	=	radius, [m]
$RANS$	=	Reynolds averaged Navier-Stokes
SS	=	Suction side
T	=	Static Temperature, [K]
TS	=	Terminating Shock
u	=	Absolute Velocity, [m/s]
UAV	=	Uninhabited aerial vehicle
X	=	Axial location, [m]
Y^+	=	Wall coordinate based on y and friction velocity
ν_T	=	Turbulent to molecular viscosity ratio
η_{ts}	=	Isentropic Efficiency (total-to-total)
Π	=	Total pressure ratio
Ω	=	Rotational rate, [rad./s] , design value=28,500 RPM

Subscripts

$B1$	=	Stator Blade 1
$B2$	=	Stator Blade 2
rot	=	Rotating frame
R	=	Rotor
S	=	Stator
TT	=	Total to total
1	=	Rotor Inlet station
2	=	Rotor Exit station
3	=	Stator Inlet station
4	=	Stator Exit station

I. Introduction

The availability of powerful multi-dimensional, viscous and rotational computational fluid dynamics tool benefits the turbomachinery field with a faster design timeline from concept-to-product. Limitations of aerodynamic design strategies with oversimplifying assumptions are effectively reduced by powerful computing resources. The advent of these tools has motivated authors to design and investigate a high-pressure ratio mixed-flow compressor for aero-propulsion purposes. It is observed that these designs were not pursued in as much detail as the axial or centrifugal compressor configurations. Based on the mean-line assessment in *Sadagopan and Camci* [1], it is clearly seen that a rotor with high flow turning and supersonic exit flow is required to generate high pressure-ratio in single stage. However, in previous efforts, the accompanying supersonic through-flow stator/diffuser performed inefficiently. To overcome this barrier designers resorted to the usage of tandem configurations to efficiently distribute the high diffuser blade loading into two blade rows, *Elmendorf et al.* [2], *Eisenlohr et al.* [3] and *Giri et al.* [4]. Even then, performance of those mixed-flow designs was limited to a total pressure ratio of 5:1 with approximately 70% efficiency. Therefore, using a tandem stator design proposed in *Quishi et al.* [5], we proceed with the challenging task of designing a high-pressure ratio stage of 6:1 within 400 mm outer diameter.

Most of the past mixed-flow compressor design performances including the current design are compared in *Sadagopan and Camci* [1]. It is observed that obtaining a high-pressure ratio and efficiency simultaneously for a single stage is quite challenging. There are only two other mixed-flow designs over the total pressure-ratio of 5:1 out of 14 past designs. Present design has the highest pressure-ratio near 6:1 at an elevated engine mass flow rate of 3.5 kg/s. There are only four past mixed-flow designs with an efficiency (η_{IS}) value over 80%. However, all those four designs exhibited a total pressure-ratio less than 3.7:1. The current design generates a pressure-ratio (Π_{TT}) of about 6:1 at an engine mass flow rate of 3.5 kg/s with a total-to-total efficiency (η_{IS}) of 75.5 %. Engine operational altitude, mass flow rate and inlet Mach number were specified as part of the input data. A stage efficiency around 75.5% is considered feasible from the preliminary mean-line design [1]. The completed solid model after the initial design efforts is shown in **Figure 1**.

From a utility perspective, combined mixed, axial or centrifugal stages can provide total pressure ratios up to 10-15 which will be quite advantageous in a turbo-shaft or turbo-fan arrangement with reduced frontal diameter. This will increase the engine's performance (thrust/weight ratio) by a significant margin. In a futuristic viewpoint, these systems could also be advantageously incorporated into the upcoming Geared-Turbo-Fan (GTF) core compressor designs [6] and the NASA distributed propulsion vehicle concept [7].

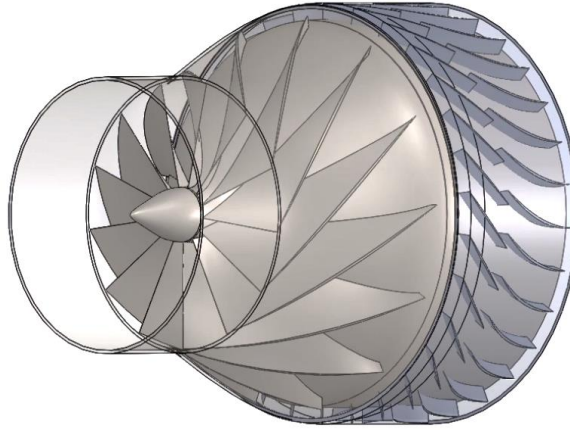


Figure 1 Mixed-flow compressor stage solid model, Sadagopan and Camci [1]

A mixed-flow compressor stage when installed in the compressor core can replace a multi-stage axial system easily. The mixed-flow approach has a great potential to shorten core compressor length. This hybrid design will involve lesser moving components hence, reducing weight, and system complexity, thus increasing the reliability factor. Another implication will be a possible reduction in manufacturing and maintenance costs. In the case of distributed propulsion systems, it can provide additional drag reduction benefits and variable duct type compact compressor application based on location of engine core along with advantages already proposed by the concept.

In this paper, we study the aerothermal characteristics of a $\Pi_{TT} = 6$ class mixed-flow compressor stage based on computational analysis. The multi-dimensional viscous/turbulent computational model is assessed against two well publicized test cases which emulate a transonic rotor and a supersonic diffuser. The experimental data sets from NASA rotor 37 [8] and RWTH supersonic tandem stator [2] are compared to the current computational results separately using RANS based simulations. The computational results show a good match against the experiments by sufficiently predicting exit profile distribution for Rotor 37 and P/P_{01} distribution for RWTH supersonic tandem stator. After validating the computational analysis code, we analyze the current $\Pi_{TT} = 6$ class mixed-flow supersonic compressor [1]. Mixed-flow rotor, 2D tandem stator and 3D stator in stage flow features are discussed in detail. Stage performance charts of this design are presented to evaluate operability of these compressors. The study highlights influence of shock wave system on stage mass flow rate, pressure and velocity distribution. A comparative study is presented between the mean-line design input data and the final computational analysis-based performance assessments. Conclusively, we assert that the current computational approach which resolves most influential compressible viscous flow features

evaluates the design point total-to-total efficiency as 77% and total pressure-ratio as 5.83 for this mixed-flow compressor design.

II. Computational model

This computational effort uses a finite volume method to transform the Navier-Stokes equations based mathematical model into a system of algebraic equations. An algebraic multigrid method is used in the general-purpose fluid dynamics solver STAR-CCM+ for approximate numerical solution. The equations are discretized in time and an implicit time-integration scheme is used to obtain quasi-steady state solution. Convective fluxes are discretized using a second order upwind scheme. A three-dimensional Reynolds Averaged Navier-Stokes (RANS) approach with one-equation Spalart-Allmaras turbulence model [9] is chosen. A performance assessment comparison using one and two-equation turbulence models on rotor alone simulation is presented in Table 2 with corresponding boundary condition in Table 5. On that basis, we proceed with Spalart-Allmaras model in the study as it accurately predicts flow features and is relatively time efficient. Calorically perfect gas condition with air as the fluid is selected. The assumption of continuum is valid since Mach no. < 3 and Knudsen no. < 1 throughout the compressor. The models described herein are used in the current fluid dynamics solver for high-speed flows [10].

A ‘coupled flow and energy model’ which couples the conservation equations for mass, momentum and energy simultaneously using a pseudo-time marching approach is used. Velocity field is obtained from momentum equations, pressure from the continuity and density from the equation of state. A time marching technique converts the unsteady derivative terms to a steady approach where those terms were driven to 0. Time step for an individual cell was evaluated based on stability constraints. This model had a robust nature for compressible fluid flows and the CPU time scaled with cell count providing good convergence with refined mesh. A Courant number of 5 was used throughout the simulations. The hybrid ‘all Y+ wall treatment’ either resolved the viscous sublayer in a fine mesh or derived wall functions from equilibrium turbulent boundary layer theory for coarse meshes without resolving the viscous sub layer. We used grid sequence initialization condition which computed the domain using an approximate inviscid solution. A series of coarse meshes were generated to interpolate solution to the next finer mesh on convergence. It provided faster and robust convergence for the flow solution as large CFL numbers could be used.

All the mixed-flow compressor simulations in this study used a single “stage” passage to minimize computational cost and time requirement by incorporating periodic boundary condition to the mid passage surfaces. The inlet is 100

mm upstream of the rotor blade leading-edge to negate upstream pressure wave effect. Outlet is 10 mm downstream to the second stator blade. All surfaces in the rotor domain rotate except the casing.

A rotor stagnation inlet condition is used for all simulations. Incoming flow direction is normal to the inlet surface. A mixing-plane rotor-to-diffuser interface is used. This mixing plane efficiently handles the rotor stator pitch differences to transfer circumferentially averaged quantities of mass, momentum and energy with uniform radial thickness. The approach significantly reduces computational time when compared to a transient simulation for turbomachinery problem [11]. The mid-passage surfaces on either side of the rotor and stator blades are utilized as periodic boundaries. At outlet for “rotor-alone” simulations back pressure at hub surface is imposed using a radial equilibrium boundary condition. For the stage simulations average back pressure at stator outlet is imposed. The values for design point are obtained from the mean-line design code explained in [1] and is given in Table 1.

Table 1 Stage boundary conditions from the mean-line analysis

Reference Pressure(P_{01}), Pa	33113.0
Inlet P/P_{01}	0.82
Inlet T_o , K	247.7842
Inlet v_T	10.0
Exit T_s , K	438.8
Exit $P_{avg.}/P_{01}$	4.98
Exit v_T	10.0

Table 2 Comparative performance assessment of rotor alone simulation for different turbulence closure models

Turbulence model	Π_{TT}	η_{is}, %	\dot{m}, Kg/s
Spalart-Allmaras	7.15	86.87	3.00
K-omega (SST)	7.16	86.80	2.92

III. Assessment of the computational method using existing compressor rotor and diffuser data

The computational system used in this study is first evaluated for its ability to reasonably predict the compressor performance using existing well-established experimental data sets. Since, main goal of this paper is to take all three dimensionalities of the stage, viscous flow effects and compressibility including the shock wave systems into account,

the authors felt that a comprehensive evaluation against existing experimental data was essential. Thus, results obtained from current steady state RANS based computational fluid dynamics solver [9] are compared to the experimental data for NASA Rotor 37 [8] and RWTH Aachen [2] supersonic tandem diffuser.

Verification 1: NASA Rotor 37 Experiment

The experimental test case of NASA Lewis/Glenn Transonic Rotor 37 from *Suder and Reid* [8, 12] is computed using the CFD model used in this study. Rotor 37 is a low aspect ratio inlet stage for an eight-stage core compressor with 20:1 total pressure ratio [12]. It serves as an ideal rotating transonic flow test case for code verification. Domain of analysis is shown in **Figure 2**. Much data representing performance and flow field variables can be found in [8] which has been used for CFD validation. Boundary conditions are obtained from *Dunham* [13] for the $0.98 \dot{m}/\dot{m}_{choke}$ condition. A stagnation pressure and temperature inlet condition is used along with average static pressure outlet. A comparison of the total pressure ratio and total temperature ratio profiles are described in **Figure 3 (a, b) and 4**. Solid circular symbols are NASA Rotor 37 experiments [8,12].

Figure 3.a and **3.b** compare the present stage exit total pressure computation against NASA Transonic Rotor 37 experiment and seven other prediction attempts that are available in open literature. Our predictions use the Spalart-Allmaras model [9] to account for turbulent flow effects. The current predictions as represented by a star symbol are in excellent agreement with the measured data denoted by solid circular symbol in the region above 75 % span. The agreement is reasonable between 30% span and 75% span when compared to all other predictive efforts. Most of the predictions including the current computational effort below 30% span are not as successful as the predictions above the mid-span.

In this effort, our CFD simulation over-predicts the total pressure deficit occurring in 0-30% span, just like all other seven predictive efforts from the literature. Hence, we decided to further investigate a possible hub leakage flow effect based on the experimental work of *Shabbir et al* [20]. A leakage flow at 0.34 % of the inlet mass flow rate is computationally examined. It is assumed to have the same total temperature as that of the free stream with 1% turbulence intensity. The leakage flow case is shown in **Figures 3.a** and **3.b** by red stars. Our current computations with no hub leakage are also represented by blue stars. *Shabbir et al.*'s work was unfortunately not conclusive in terms of accounting for the total pressure overpredictions near hub region below 30% span. They varied the leakage rate in a wider range and that hub leakage influence did not resolve the usually observed predictive anomaly in 0-30%

span. Our current effort with hub leakage resulted in a very similar total pressure profile in the spanwise direction when compared to the no-leakage case as shown in [Figures 3.a and 3.b](#). Only a slight difference near the hub was observed between no-leakage and leakage cases.

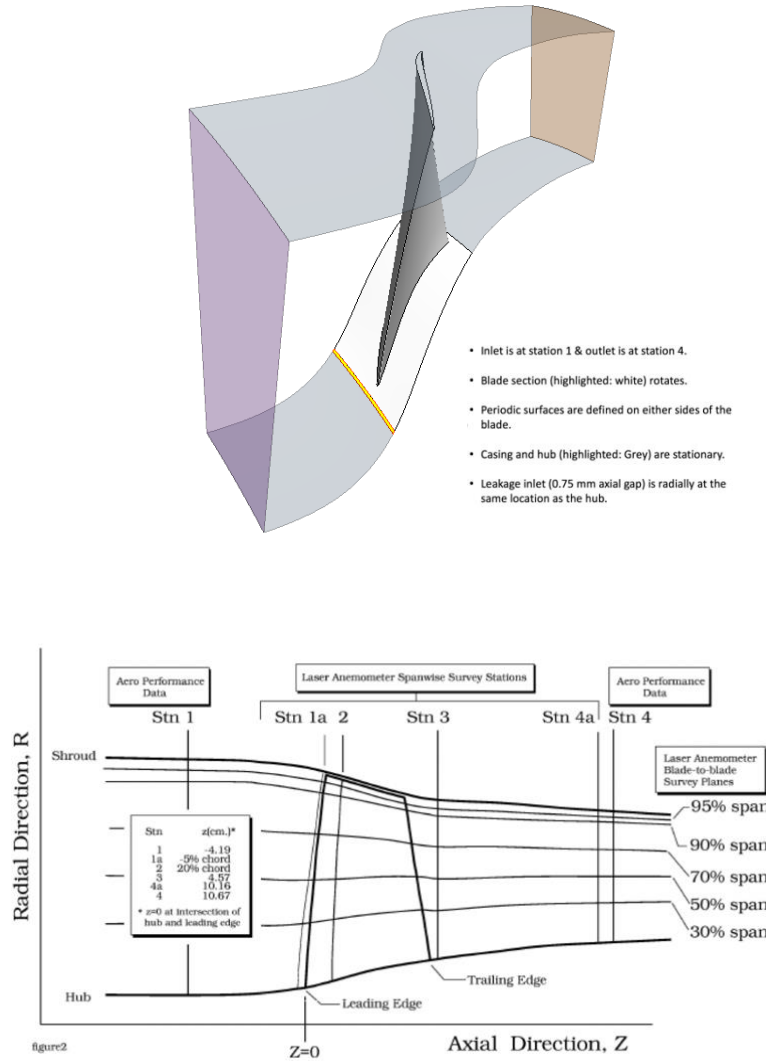
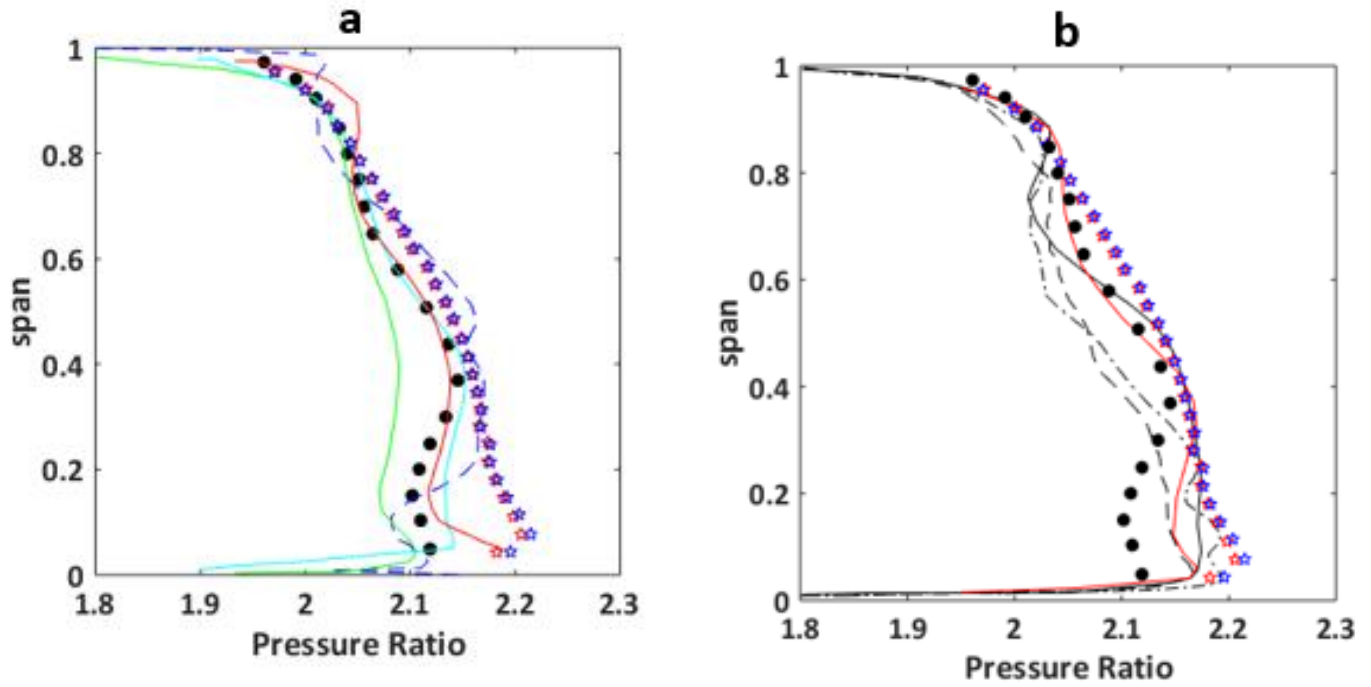


Figure 2 Geometry of NASA transonic rotor 37 experiment and computational domain.

The authors also investigated rotational effects of the entire hub. However, based on those results two reasons were inferred to negate this possibility. Firstly, results did not vary compared to the rotating blade section results in terms of overprediction of total pressure below the 30% span. Secondly, rotating the entire hub would induce more energy into the flow through shearing effects which will add on to total pressure overprediction. Moreover, it is important to note that the original experiment did not have entire hub rotating.



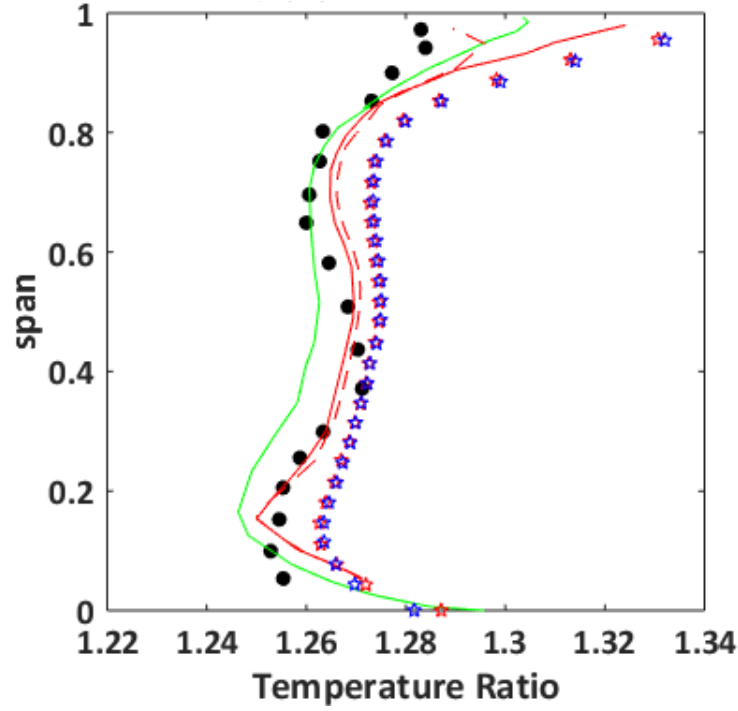
	Investigators	Analysis type
●	Suder [8]	Experiment
☆	Sadagopan and Camci*	RANS, No hub leakage
★	Sadagopan and Camci*	RANS, With hub leakage
*Present computation		
3.a		
---	Hah, C. [14]	LES
---	Ameri, A. [15]	RANS
---	Boretti, A. [16]	RANS
---	Bruna and Turner [17]	RANS
3.b		
---	Joo, J. et al [18]	RANS, trip
---	Joo, J. et al [18]	LES ₀
---	Joo, J. et al [18]	LES _{nal}
---	Seshadri, P. et al [19]	RANS

Figure 3 (a, b): Total pressure ratio distribution in the span-wise direction at station 4 for $\dot{m}/\dot{m}_{choke}=0.98$ (Experiments are from Suder [8])

The most effective and more recent simulation of NASA Transonic Rotor 37 was performed by *Bruna and Turner* [17] in the near hub region. CFD simulations were obtained with an isothermal thermal boundary condition for running NASA Rotor 37 case in contrary to all other simulations in the literature. All past simulations in **Figures 3 (a, b)** and

4 used an “adiabatic wall” boundary condition. Their simulation [17] was also repeated using an adiabatic boundary condition. The red solid line for the isothermal wall boundary condition in Figure 4 matched the experimental data remarkably well. This is the best prediction of the total pressure distribution for Rotor 37 in the literature. Although their total pressure, temperature and stage efficiency calculated matched very well with experimental data, Bruna and Turner [17] observed and claimed that the real compressor rig experiment would not be isothermal at the casing. A proper analysis would require a conjugate heat transfer approach. In their simulation, entire hub rotated. They noted that cavities existing in the hub region needed to be modeled for better prediction. They [17] reported that the computed efficiency data using an isothermal boundary condition matched experimental data much better than the adiabatic simulation. The efficiency difference between isothermal and adiabatic solutions was about 1%. Figure 4 shows Bruna and Turner’s total temperature prediction ability at stage exit. The profiles of total temperature with isothermal boundary condition matched very well with the data near casing. All past adiabatic simulations have an overshoot that has consistently been a part of CFD versus experimental data comparison. The total temperature prediction from current work reasonably compares with the experimental data.

The present computational verification effort resulted in predicting stage exit total pressure and temperature ratios that are better or very similar to most of the past Rotor 37 computations. The near hub region below 30 % span is still an area of uncertainty, in terms of thermal boundary condition. This effort proceeds with an adiabatic type thermal boundary condition. However, implementation of a conjugate heat transfer model is likely to be a topic of future investigation. It is current authors’ observation that present computational approach can be effectively utilized to predict transonic/supersonic compressor rotor flow fields to develop better mixed-flow compressors.



Symbol	Investigators	Analysis type
●	Suder [8]	Experiment
☆	Sadagopan and Camci*	RANS, No hub leakage
★	Sadagopan and Camci*	RANS, With hub leakage
*Present computation		
—	Ameri, A. [15]	RANS
—	Bruna and Turner [17]	RANS, adiabatic
- -	Bruna and Turner [17]	RANS, Isothermal

Figure 4 Total temperature ratio in the spanwise direction at station 4 for $\dot{m}/\dot{m}_{choke}=0.98$.
(Experiments are from Suder [8])

Verification 2: RWTH, Aachen Supersonic Tandem Stator Experiment

The current computational method's ability to resolve aerothermal characteristics of a supersonic diffuser with shock wave systems is assessed using experimental data from RWTH, Aachen supersonic tandem diffuser, [2]. This is a two-dimensional simulation. The design point operating boundary condition obtained from Elmendorf et al. [2] is given in Table 3. Figure 5 shows the tandem diffuser geometry in a linear cascade arrangement. Blade '1' inlet region has a straight contour to avoid excessive flow acceleration and is followed by a locally divergent region to position the strong shock stabilized by back pressure. Blade '2' is introduced to keep the subsonic flow diffusion at moderate levels.

Table 3 RWTH Aachen tandem diffuser boundary conditions

Reference Pressure(P_{o1}), Pa	126300.0
Inlet Mach number	1.478
Inlet P/P_{o1}	1.836
Inlet T_o , K	559.12
Exit Mach number	0.368
Exit P/P_{o1}	4.30
η_{is}	72.09%

The current computations compare computed blade ‘1’ airfoil surface static pressure distribution (P/P_{o1}) to RWTH experimental data in [Figure 5](#). Multiple static pressure jumps visible in the figure correspond to shocks. Inlet supersonic flow generates a weak oblique shock at the leading-edge of blade ‘1’. This flow slightly accelerates on the pressure and suction side of blade ‘1’. The pressure side leg of oblique shock impinges on the suction side at ‘B’. A convergent passage leads to a strong shock from ‘A’ to ‘C’ which has higher strength on the pressure side. A complex shock structure is formed near the leading-edge of blade ‘2’. The convex suction side of blade ‘2’ generates extreme acceleration of the flow leading to another strong shock extending to the concave pressure side of blade ‘1’ as shown in location ‘D’. There is a slight discrepancy in the shock location and magnitude of ‘D’ when compared to experimental data. This variation is due to a subtle geometrical variation in blade ‘2’ which could not be captured with high enough resolution while generating the current grid system from information published in [\[2\]](#). The strong passage shock at ‘D’ increases static pressure tremendously. An isentropic efficiency of 72.09 % is predicted for this diffuser. There is a very good agreement between the measured data and current computations between $X/L_{B1}=0.4$ and 1.0 for blade ‘1’. Even though this region is located just downstream of a very complex set of shock waves, the current predictions effectively capture the measured diffuser pressure distribution. There is no experimental pressure data available for blade ‘2’ after X/L_{B1} . Although there is a limited number of wall static pressure measurements before $X/L_{B1}=0.4$, the current predictions follow the measured wall static pressure points closely. This area is dominated by a weak oblique shock, a stronger passage shock between A and C. When the complex interactions of these shock waves with the boundary layers and other flow features are considered, the predictions that are shown in [Figure 5](#) follow the experimental trends very well. It should be noticed that the experimental data will have a certain amount of uncertainty that is not documented in [\[2\]](#).

Conclusively, computational assessments presented in [Figure 2-5](#) showcase the nature of CFD based performance predictions against two well established high-speed flow cases existing in open literature. Thus, we proceed with this computational model which can successfully capture general features of a three dimensional, viscous, compressible and turbulent flow suitable to assess and analyze performance of a supersonic mixed-flow compressor [\[1\]](#).

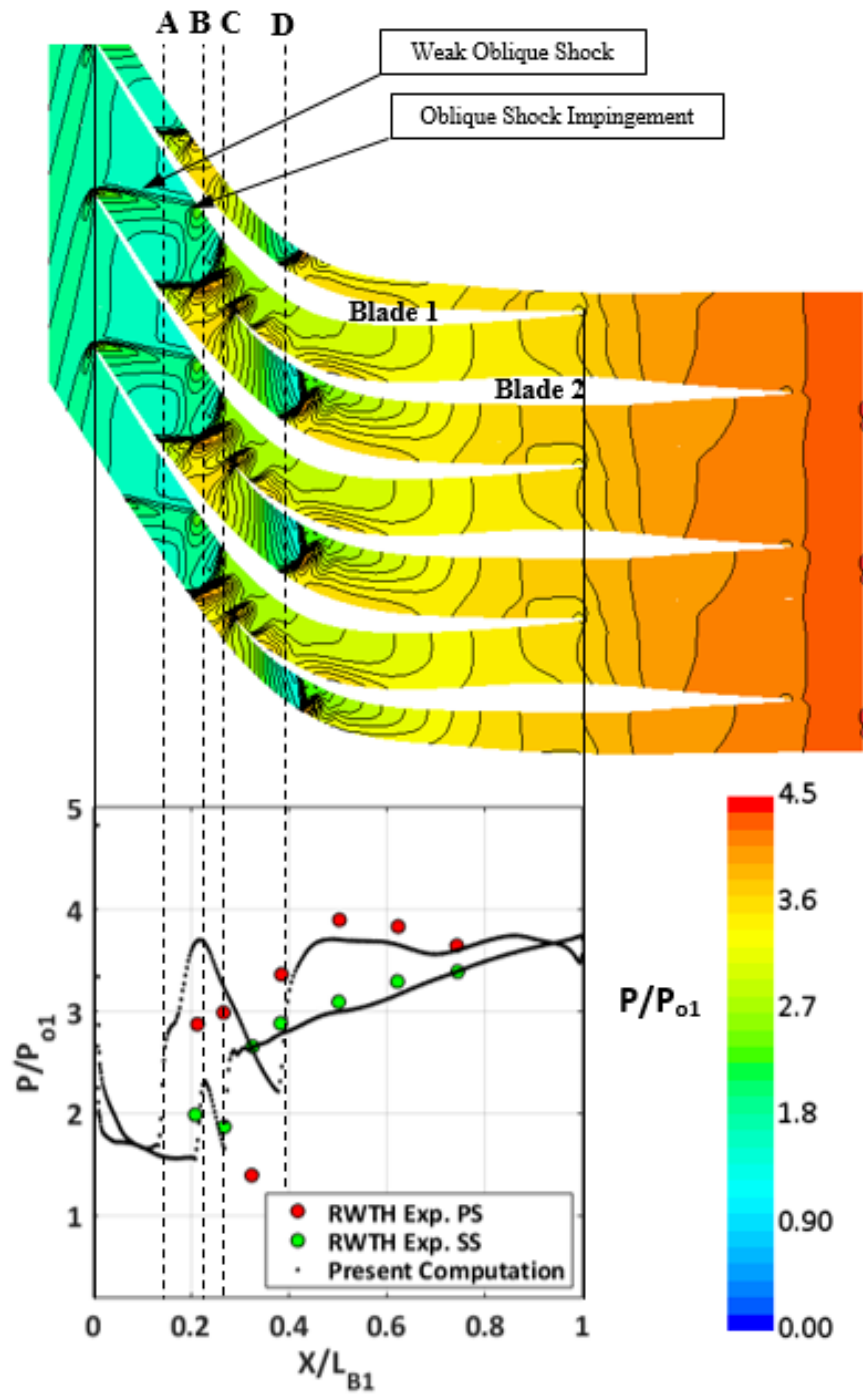
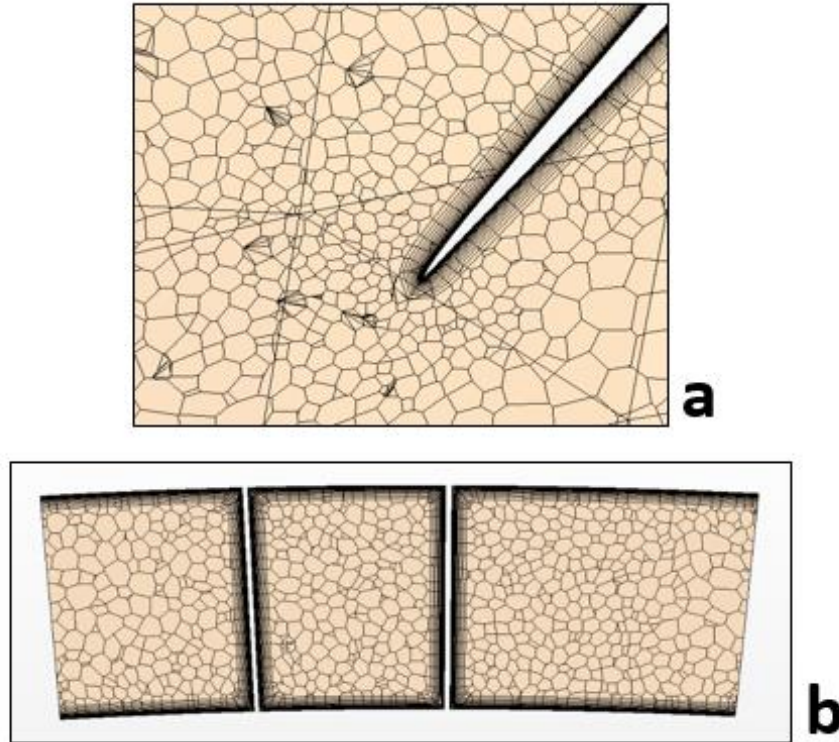


Figure 5 CFD vs experimental data comparison for the RWTH, Aachen tandem stator cascade.

IV. Mesh dependence study for the current predictive effort

The mesh measure of a finite-volume based RANS computation influences quality of its viscous and compressible flow predictions. Therefore, it is essential to quantify mesh dependency of the computations. An automated meshing tool built into the current fluid dynamics solver [10] is used to generate unstructured polyhedral cells for discretizing the fluid domain. Base cell size on the fluid domain surfaces is specified to construct this polyhedral mesh. These polyhedral cells are further discretized into orthogonal prismatic cells next to the wall surfaces to improve flow resolution inside boundary layers. Typical sectional views of representative grid zones are shown in Figure 6 (a, b) and the mesh property inputs are presented in Table 4. A rotor fluid-domain only simulation is performed for undertaking the mesh dependence study with three different types of meshes (coarse, moderate and fine). The same set of boundary conditions given in Table 5 is used for all three cases. All except the coarse type mesh, had prismatic cells sufficient enough to maintain a $Y^+ < 1$ at all grid points adjacent to the wall. Base cell size on casing, hub and blade walls were reduced to increase passage resolution progressively from coarse to fine mesh.



*Figure 6 Polyhedral mesh detail at the moderate level with prism layer (boundary layer) cells:
a. Rotor leading-edge, b. Stator mid chord plane.*

Rotor blade static pressure C_p distribution at 65% span plotted in [Figure 7](#) clearly shows influence of mesh size on providing passage shock resolution for all the 3 meshes. Leading-edge acceleration on both pressure and suction side is depicted by a C_p drop near $X/L_R=0$. Expansion fans generated on the suction side (SS) is observable for all three mesh resolutions, between $X/L_R=0$ and 0.05 . Further downstream on the SS, a weak shock influence is shown by the gradual increase in C_p observed before $X/L_R=0.10$. This shock on the SS generates a separation bubble due to shock boundary layer interaction. The rotor passage shock observed in coarse mesh case is wider as its spread over relatively larger cells.

The coarse mesh computation has a passage shock with higher strength and is initiated later than the other cases ending near $X/L_R=0.37$ on the SS. This variation could be easily attributed to the absence of boundary layer resolution prolonging the SS acceleration and a coarser grid predicting wider area of shock influence. This apparent transition in shock location is observed directly as a mass flow rate increment as shown in [Table 6](#). Inlet Mach number (M_I) shown in [Figure 8](#) also supports this case. Beyond $X/L_R=0.37$ on the suction side, C_p trend on the rotor airfoil is similar for all 3 mesh resolutions. On the pressure side, shock influence in coarse grid disappears after $X/L_R=0.15$. The sudden drop of C_p on SS beyond $X/L_R=0.9$ is due to “casing” region separated flow zone interaction near rotor exit.

The stagnation pressure at rotor outlet for the 3 cases is shown in [Figure 9](#). For both moderate and fine meshes, it is very close within a $\Pi_{TT}=\pm 0.15$ for most span-wise locations. The coarse mesh contains shock influenced areas that are unrealistically spread over larger zones. The predicted efficiency value for coarse mesh is higher than the other two cases by about 3 % as seen in [Table 6](#), and [Figure 10](#).

[Table 6](#) clearly specifies that performance evaluation of both moderate and fine mesh is very close to each other. The former case being computationally time efficient, authors infer to use moderate mesh throughout the mixed-flow compressor computational effort.

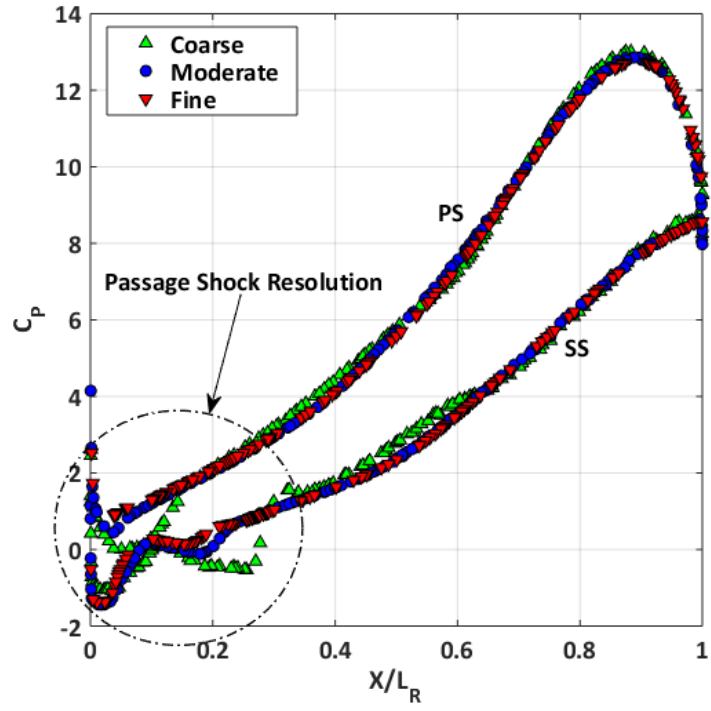


Figure 7 C_p distribution at 65 % rotor blade span for the 3 types of mesh measure.

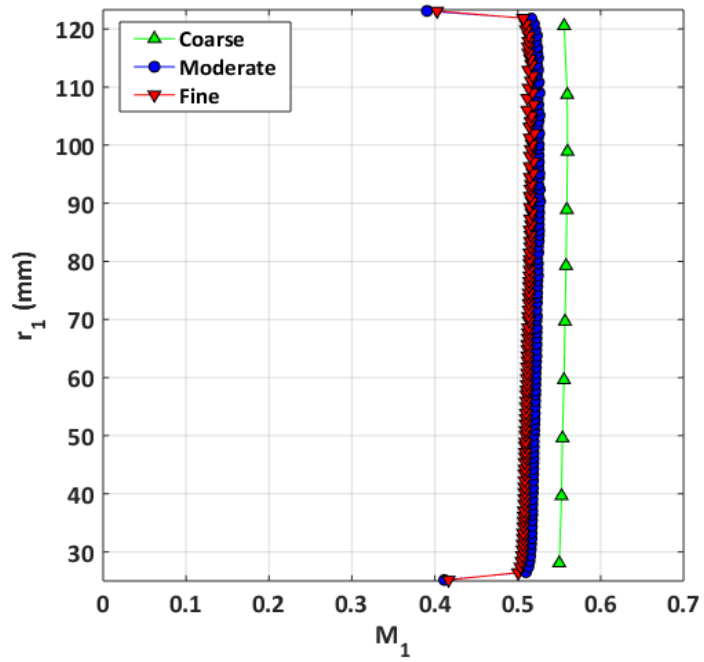


Figure 8 Rotor inlet Mach number, M_1 for coarse, moderate and fine mesh. (Circumferentially mass averaged)

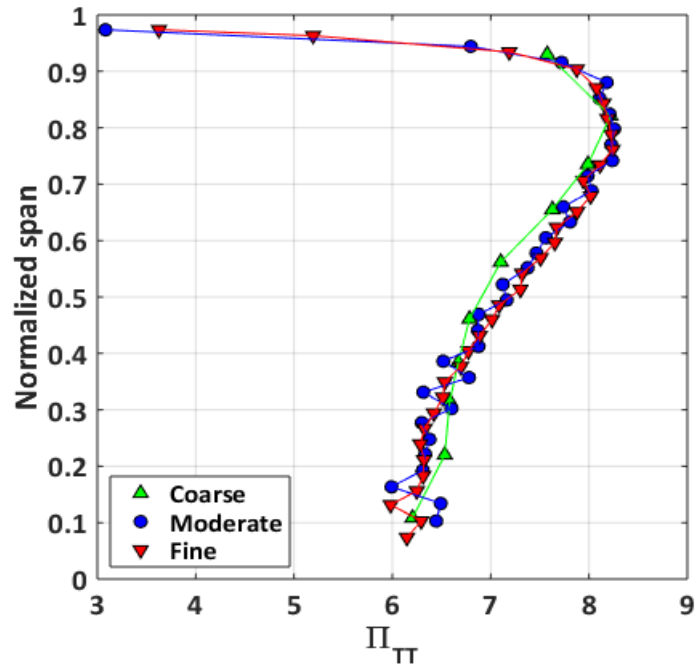


Figure 9 Stagnation pressure $\Pi_{TT} = P_{o2}/P_{o1}$, coarse, moderate and fine mesh at rotor exit, 150 mm
(Circumferentially averaged at rotor exit)

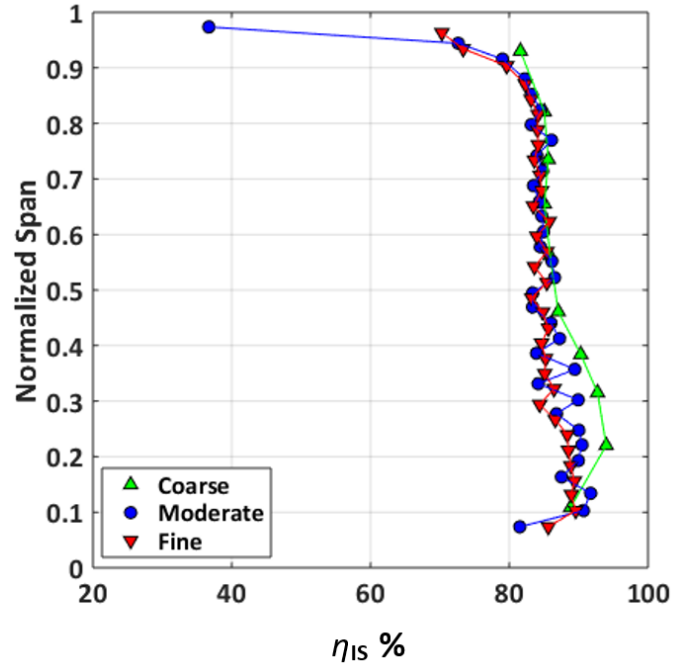


Figure 10 Isentropic efficiency at rotor exit for coarse, moderate and fine mesh at rotor exit, 150 mm.
(Circumferentially averaged at rotor exit)

Table 4 Mesh input data comparison between coarse, moderate and fine cases

Mesh Property definition	Coarse	Moderate	Fine
Polyhedral mesh	Yes	Yes	Yes
Prism Layer (Boundary layer mesh)	No	Yes	Yes
Base cell size - rest of the domain(mm)	3	2.1	0
Base cell size - wall (mm)	0.99	0.99	0.3-0.6
No. of prism layers	N/A	25	25
Total prism layer thickness (mm)	N/A	0.99	0.99
Stretching factor (Geometric Progression)	N/A	1.2	1.2
Wall proximity distance (mm)	N/A	0.001	0.001
Total no. of cells (in millions)	0.1	3.1	12

Table 5 Rotor only simulation boundary conditions

Reference Pressure (P_{o1}), Pa	33113.0
Inlet T_o , K	247.78
Inlet v_T	10.0
Exit T_s , K	320.98
Exit $P_{avg.}/P_{o1}$	2.474
Exit v_T	10.0

Table 6 A comparative assessment of mesh dependency with one-equation turbulence model

Mesh	No of cells	BL	\dot{m} , Kg/s	η_{IS} %	Π_{TT}
Coarse	0.1 million	No	3.129	89.27	7.13
Moderate	3.1 million	Yes	3.000	86.87	7.15
Fine	12 million	Yes	2.960	86.49	7.15

V. Rotor flow features

Rotor flow features at design point are analyzed in a rotor alone simulation using high-resolution 12 million cell mesh. The fluid-domain has the stagnation inlet 100 mm upstream of the leading edge and the average pressure outlet 10 mm downstream of the rotor trailing edge. Boundary conditions of this simulation are given in [Table 5](#). Dominant viscous flow and shock interaction related structures triggering aerodynamic losses are highlighted in this description. Some light is also shed on the typical mixed supersonic rotor flow configurations.

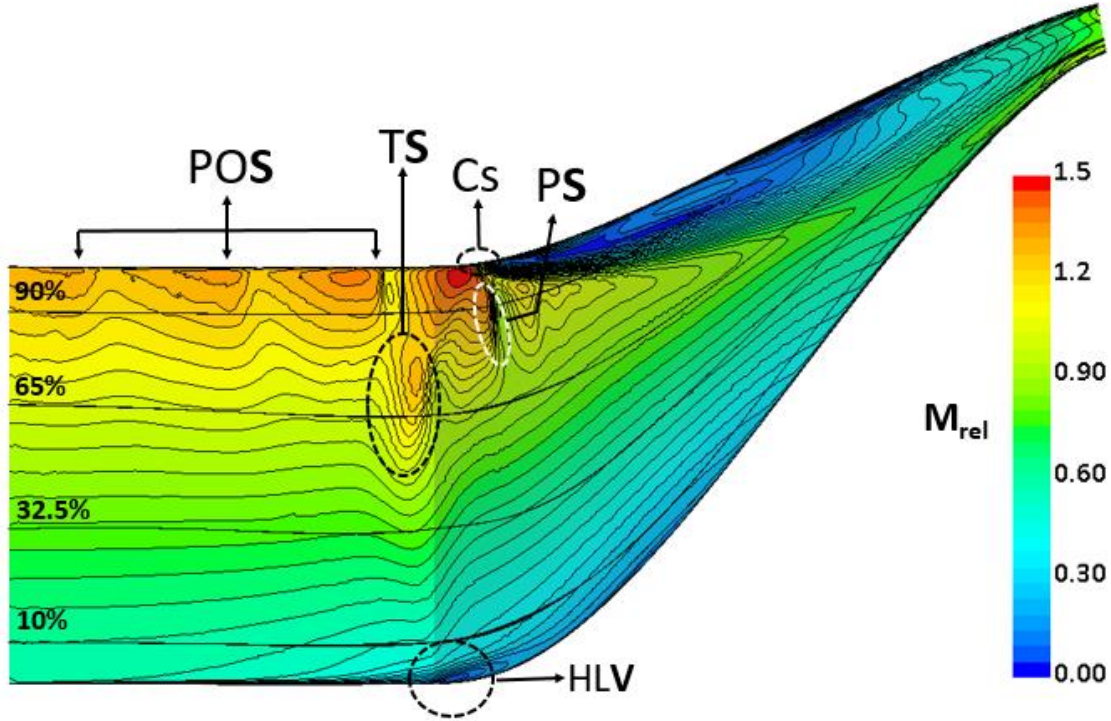


Figure 11 Meridional view of relative Mach number distribution showing the flow features at the design point: POS - Passage oblique shock; TS - Terminating shock; Cs - Casing BL separation; PS - Passage shock; HLV - Hub leading-edge vortex

Casing shock boundary layer separation ‘Cs’ is the most severe loss creating flow feature creating a low momentum zone which extends for at least 60% of the passage length as seen in [Figure 11](#). This flow separation is fully corroborated by the shock stabilization condition, [eqn.1](#), derived based on conservation of mass and energy [\[22\]](#). It states that flow is stable in zones where the area derivative (LHS left hand side of equation 1) exceeds the speed line derivative (RHS right hand side of equation 1). This condition should be satisfied to obtain shock structures that are stable across the passage for different rotational rates as given in [Figure 12](#). Speed line derivative of [eqn. 1](#) (dashed lines) exceeds the area derivative (solid line) in $\mathbf{X/L_R} = 0.1 - 0.18$ range. Meridional Mach number distribution clearly shows flow separation near $\mathbf{X/L_R}=0.1$ location. Further downstream another unstable zone occurs at $\mathbf{X/L_R} = 0.70$. Flow accelerates in the relative frame beyond $\mathbf{X/L_R} = 0.70$ mark.

$$\frac{\partial}{\partial x} \left(\frac{A}{A_1} \right) \geq \frac{\partial}{\partial x} \left[\frac{\frac{2C_p T_{rot} + 1}{u_1^2}}{\frac{2C_p T_{rot} + \left(\frac{u}{u_1} \right)^2}} \right]^{\frac{\gamma+1}{2(\gamma-1)}} \quad (1)$$

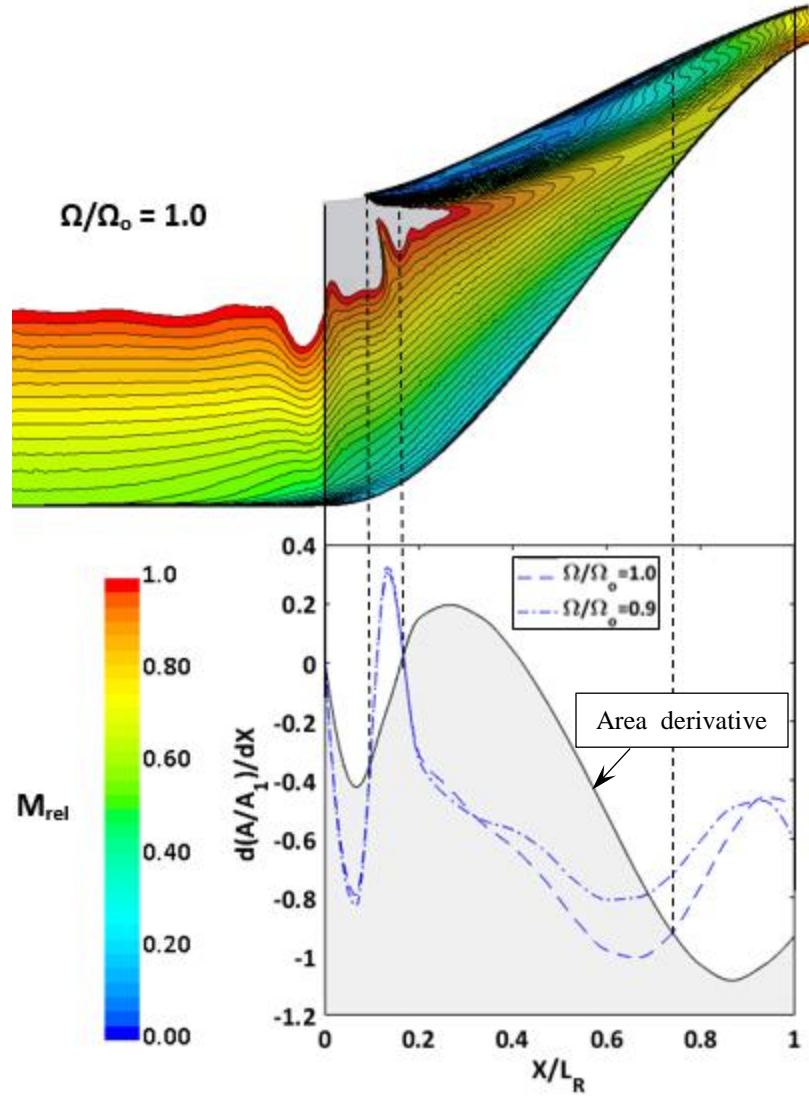


Figure 12 Shock stability analysis using eqn. 1 in the rotor passage and the corresponding computational relative Mach number distribution.

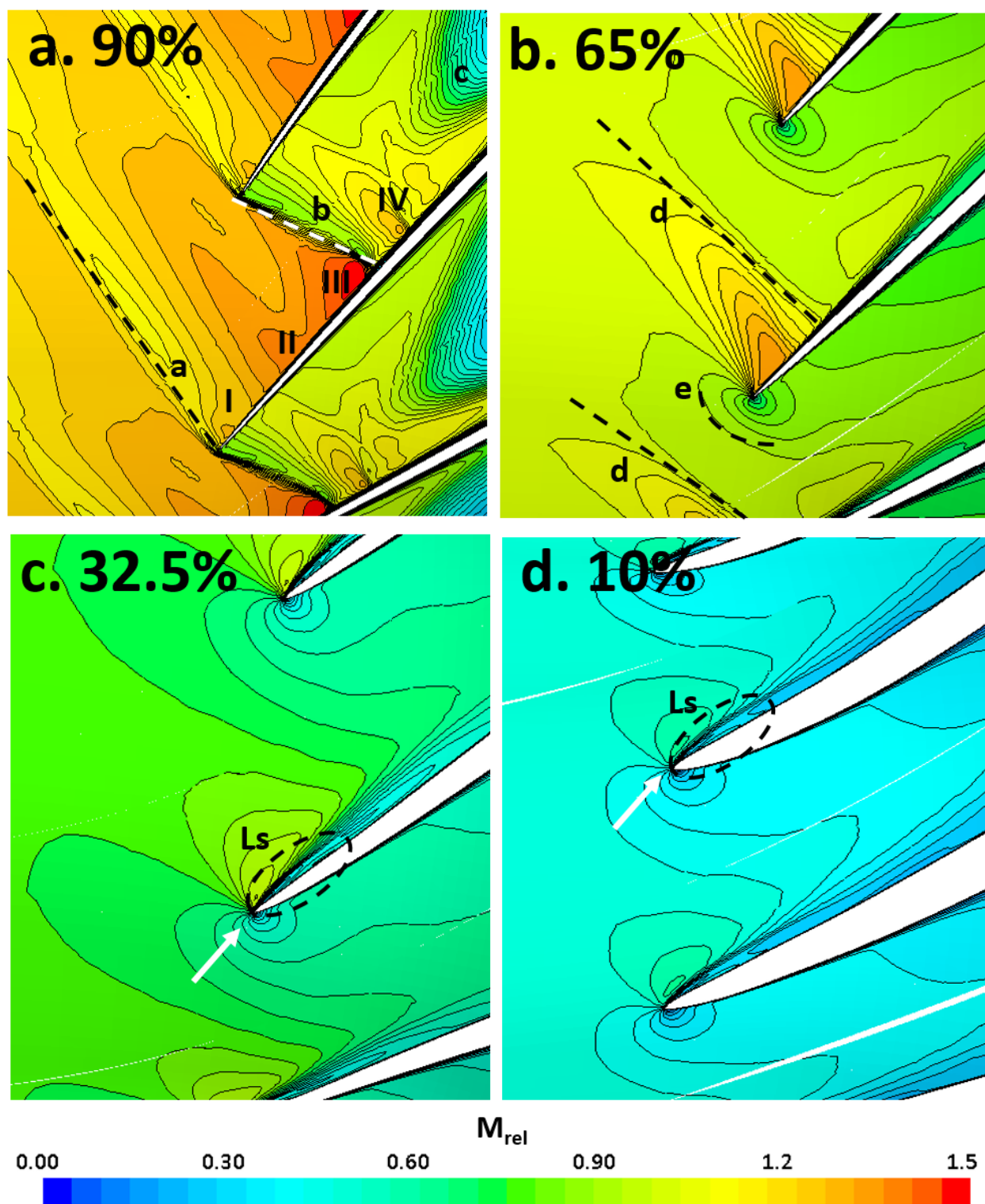
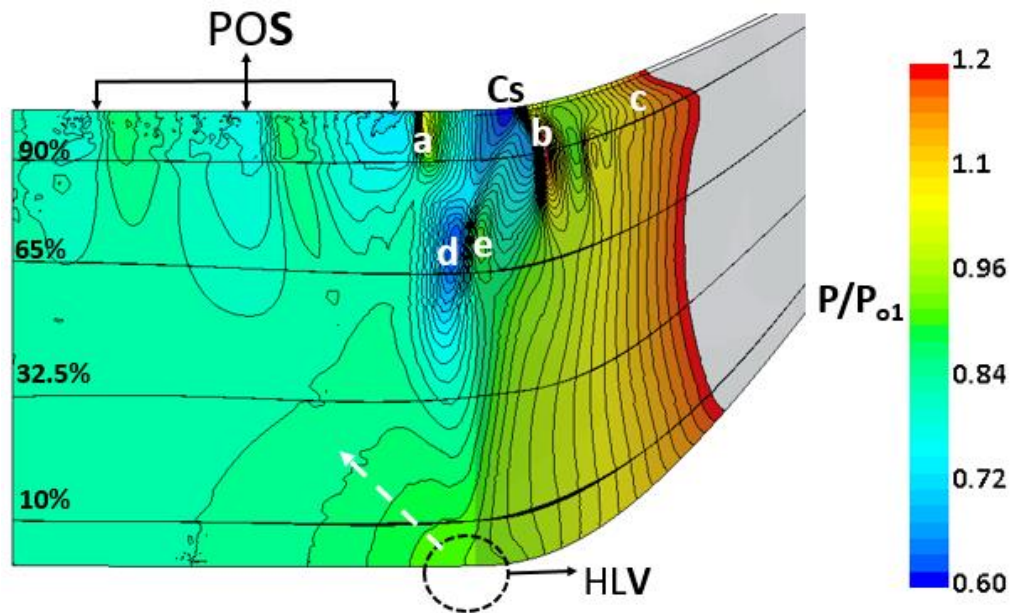


Figure 13 Relative Mach number distribution at a: 90%, b: 65%, c: 32.5%, d=10% span at the design point.
Ls – Leading edge separation

Relative Mach number contour across the rotor passage at 90 % span is shown in **Figure 13 (a)**. M_{Irel} in **90-100% span** near the tip region is supersonic with values around 1.3-1.4. At this M_{Irel} a wedge shaped leading-edge generates attached oblique shocks. Inlet freestream flow encounters a series of compression and expansion zones due to these oblique shock waves from neighboring blade passages before reaching the leading-edge as shown by 'POS' in **Figure 14**. Suction side leg of the attached oblique shock 'a' extends into inlet freestream whereas pressure side leg forms the passage shock 'b'. On the suction side as seen in **Figure 13 (a)** flow accelerates due to expansion fans 'I and II', due to a viscous boundary layer growth over convex surface. These fans reflect back from the sonic line as compression waves. As the shock is weak, it reattaches and then accelerates. A third set of expansion fans 'III' forms stronger shock which extends across to the pressure side of neighboring blade as a passage shock 'b'. Boundary layer on suction side is detached due to strong nature of this shock wave. Another set of expansion fans 'IV' are formed due to convex boundary layer. It leads to a set of weak reattached flow zones. Finally, the flow merges into a low momentum zone 'c' which exists due to casing shock boundary layer separation marked as 'Cs'. Blade loading diagram in **Figure 17** clearly shows these features in the 90% span. A gradual decrease and increase in C_p signifies the expansion fans and compression waves whereas the sudden increment corresponds to the shocks.



*Figure 14 Pressure distribution meridional view at the rotor design point:
POS – Passage oblique shock; Cs – Casing shock-BL separation; HLV – Hub leading-edge vortex.*

M_{Irel} is around 1 at 60% span as seen in **Figure 13 (b)**. The rotor leading-edge behaves like that of a transonic airfoil in **60-90% span**. Leading-edge in this span has a finite radius which generates stagnation region due to deceleration caused by terminating shock waves 'TS'. As observed in the 90 % span, inlet flow passes through a series of compression and expansion zones due to the suction side terminating shock waves 'd'. As flow is decelerated to subsonic flow behind the shock, a stagnation zone 'e' prevails observed as 'TS' in **Figure 11**. Suction side acceleration generates an expansion and compression region 'V' in **Figure 13 (b)** which is terminated by the shock wave 'd'. This flow further downstream of the shock prior to merging with low momentum zone of casing separation, behaves like a subsonic compressor passage.

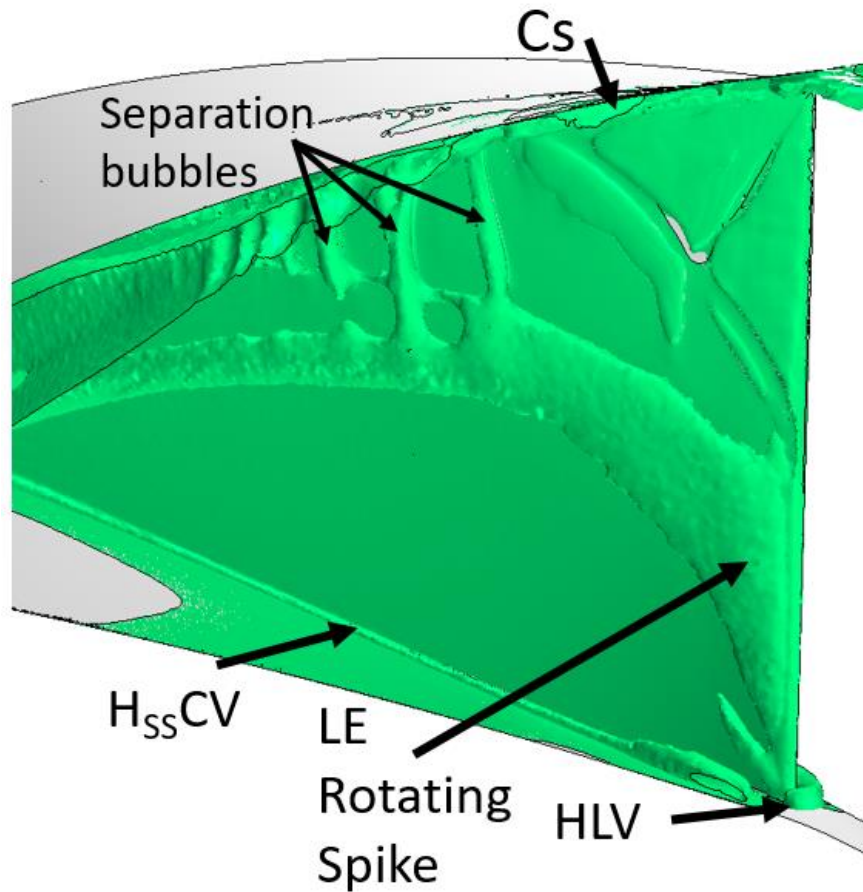


Figure 15 Rotor blade suction side vortex visualization using Q-criterion

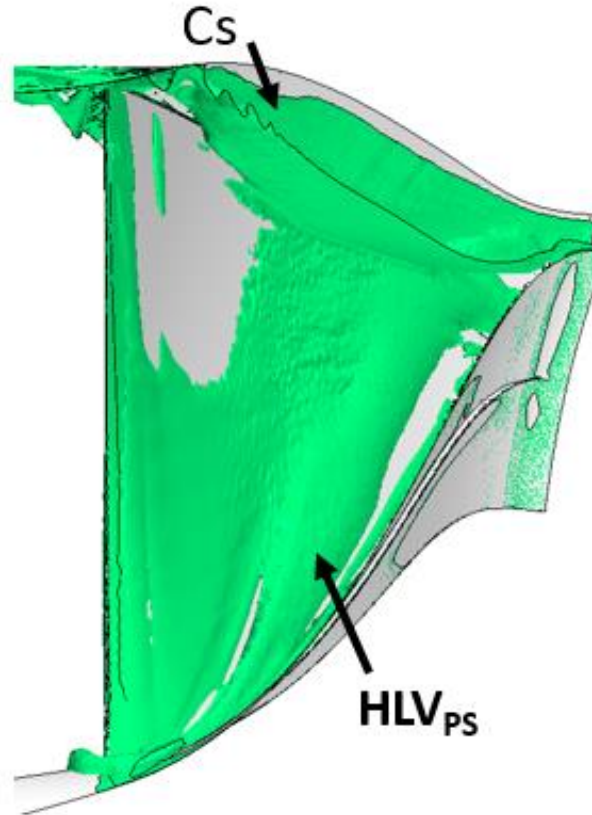


Figure 16 Rotor blade pressure side vortex visualization using Q -criterion

The inlet hub boundary layer generates typical leading-edge horse shoe vortices ‘HLV’ on encountering blade leading-edge as shown in [Figure \(15-16\)](#). This re-circulatory flow feature extends on both suction and pressure sides near the leading-edge hub junction. Both the suction and pressure side hub corner vortices ‘ $H_{PS}CV$ ’ and ‘ $H_{SS}CV$ ’ are visible which extend throughout the passage [Figure 15](#). The subsonic inlet flow in 0-30% span decelerates due to an increment in pressure created by ‘HLV’. This effect is observed in [Figure 14](#). Incidence angle of relative inlet flow increases shifting the stagnation point and causing a leading-edge separation (Ls) on the suction side as observed in [Figure 13 \(d\)](#). Rotor leading-edge region for the 30-60 % span behaves like a high subsonic flow airfoil seen in [Figure 13 \(c\)](#). Incidence effects cause flow separation on the suction side. Leading-edge separation in the 0-60% span manifests as a rotating spike structure [\[23\]](#) which travels all through the passage near the suction side to join the low momentum zone as seen in [Figure 13 \(a\)](#). Tip leakage vortex is dominant near the leading-edge of rotor blade. It mixes with the low momentum zone. On the pressure side ‘ HLV_{PS} ’ raises over blade tip and mixes with the low momentum zone as a leakage flow.

Blade loading distribution at 10 (hub), 65 (mid) and 90 (tip) % span for the rotor is shown in [Figure 17](#). It shows that a higher loading in hub frontal section due to over bending of the blade will lead to suction side flow separation causing reduction in efficiency. For the hub line near leading-edge, centrifugal force cannot generate high-pressure ratio as the meridional passage height is not increasing abruptly. Therefore, as the hub line height increases in posterior side any loading increment in this zone will enhance pressure rising capability. Conversely, for the tip region, higher loading near the frontal section will increase rotor's pressure rising ability and a decreased loading in the tip posterior section will help in controlling the inevitable suction side separation of tip region. Conclusively, based on *Xuanyu et al. [24]* increasing hub loading makes impeller achieve higher performance with lower tip leakage loss and uniform flow outlet at exit. Increasing tip loading makes the impeller achieve a higher-pressure ratio.

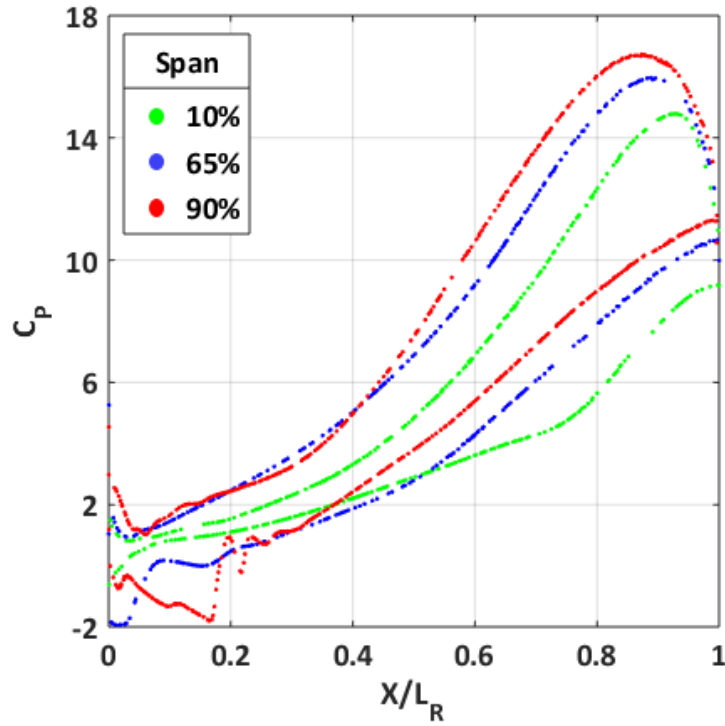


Figure 17 Blade loading distribution along blade meridional chord for 10, 65 and 90% rotor span at design point.

VI. Stator Flow Features

This computation aims towards the visualization of shock wave system for a tandem stator [\[1\]](#) having a constant radius from inlet to exit. Thus, **two-dimensional** computational simulation of the tandem stator configuration is evaluated as shown in [Figure 18](#). [Table 7](#) shows the corresponding boundary condition. **Inlet boundary condition is**

obtained from mixed-flow rotor exit data. An oblique shock is created on encountering the leading-edge of blade '1'. Pressure side leg of the shock impacts on the suction side whereas the suction side leg diffuses into the flow. Suction side acceleration is obstructed due to impinging passage shock. This shock generates flow separation zones on PS and SS locations due to shock-boundary layer interaction. Flow turning is limited in 7-10° range for blade '1' to avoid excessive separation losses as it is the most dominant loss creating mechanism. Leading-edge SS of blade '2' is placed near the trailing edge PS of blade '1'. The low momentum separated flow of shock-BL interacts with blade '2's accelerating flow on the suction side to diffuse that generated wake. Subsonic blade '1' exit flow is perfectly aligned for the second blade. The second blade row provides subsonic diffusion along with high flow turning in 40-50° range. These effects are evident in the C_p distribution.

Although initial flow visualization is performed as a two-dimensional stator computation, final performance computations for the mixed flow compressor stage are performed on a three-dimensional stator. It is important to note that the stator inlet flow is almost two-dimensional in nature as shown in [Figure 23](#). Performance comparison of 2D stator alone and 3D stator in stage simulations with same inlet boundary condition and shock structures are presented in [Table 8](#). [Figure 19](#) describes the corresponding P/P_{o1} comparison between the mid-span 3D and 2D stator computations. It is inferred that static pressure rise in 3D stator is lower than 2D stator. The authors conclude that a 2D stator alone simulation is highly efficient and effective in predicting constant radius 3D stator's shock structure and performance. It is concluded that the current design fully described in [\[1\]](#) performs better than previous supersonic tandem stator designs [\[2\]](#), [\[3\]](#) and [\[4\]](#) when the inlet Mach number is in 1.1-1.4 range.

Table 7 Current tandem stator 2D CFD boundary conditions

Reference Pressure($P_{ref.}$), Pa	88844.5
Inlet Mach number	1.2315
Inlet $P_o/P_{ref.}$	2.528
Inlet T_o , K	456.64
Exit Mach number	0.4407
Exit $P/P_{ref.}$	2.031
η_{is}	90.1%

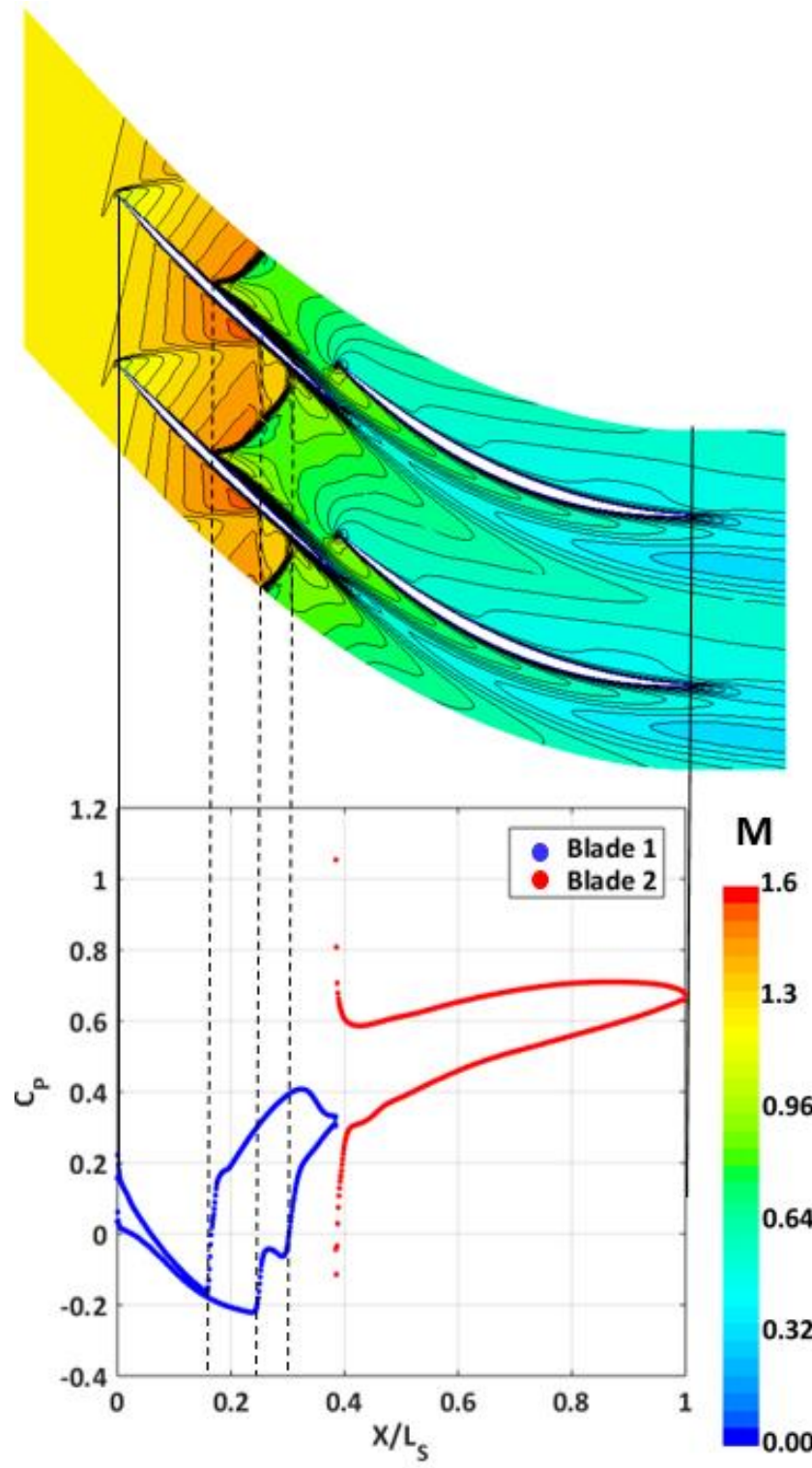


Figure 18 Current tandem stator blade loading and corresponding Mach number contour

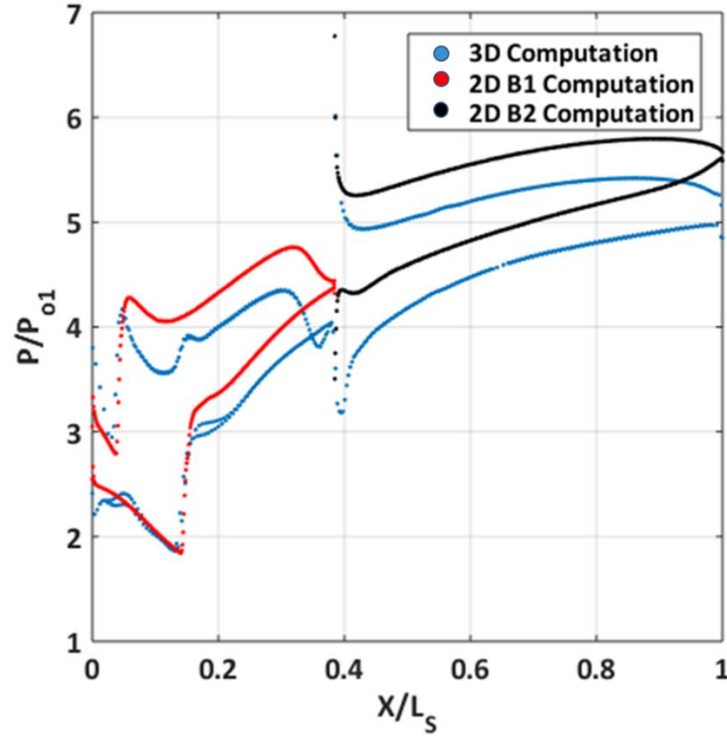


Figure 19 Static pressure rise comparison between mid-span 3D stator in stage and 2D stator alone simulation for the same inlet boundary condition and similar passage shock structure.

Figure 20 represents entropy generation of the comparative assessment 2D stator alone simulation. ‘A’ highlights the viscous losses occurring due to boundary layer growth. ‘B’ represents the weak passage shock. ‘C’ defines the shock-boundary layer interaction creating a flow separation. This phenomenon generates the highest entropy as inferred from the computational assessment. Downstream of the separation point, this low momentum flow infuses with high momentum blade row ‘1’ passage flow and aspirated flow between blade ‘1’ and ‘2’. The generated wake diffuses, and this behavior is clearly seen at point ‘D’ as entropy values reduce. Finally, excessive flow turning in blade row 2 suction side leads to mild flow separation at point ‘E’.

Table 8 Performance comparison between 2D stator alone and 3D stator in stage simulations.

	M_3	M_4	Total Pressure recovery (P_{04}/P_{03})	η_{1s} (%)	P_4/P_3	Diffusion factor (based on Lieblein (1953))
2D (alone)	1.313	0.42	0.92	90.76	2.287	0.73
3D (stage)	1.308	0.457	0.85	90.12	2.184	0.71

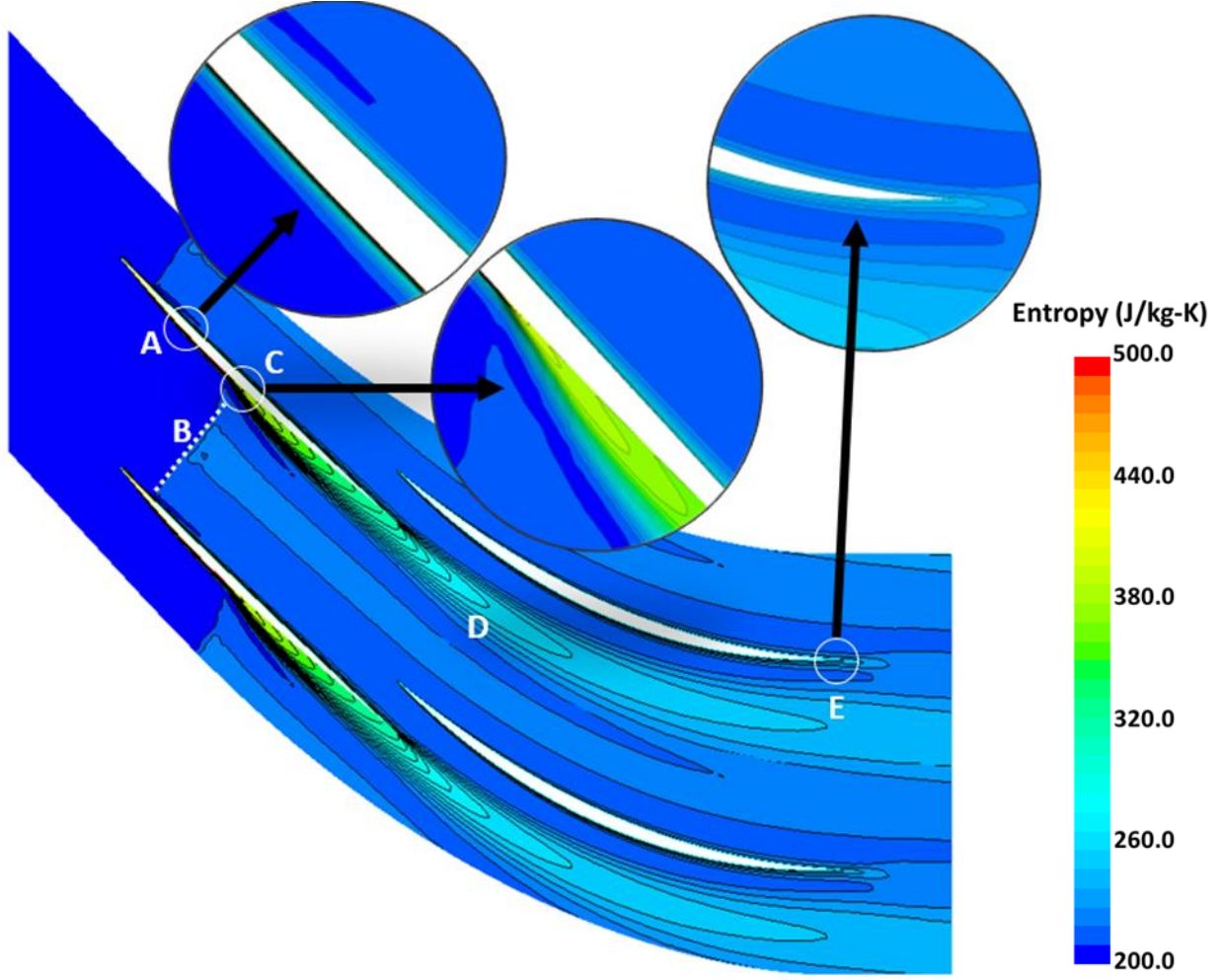


Figure 20 Entropy generation across the 2D tandem stator based on computational effort

VII. Stage Performance

Performance charts of the supersonic mixed-flow compressor stage is shown in [Figure 21](#). The design goal of $\Pi_{TT} = 6.0$ is marked as the dashed horizontal line. At the rotor design speed this compressor stage reaches a maximum Π_{TT} of 5.83 with 77% efficiency at 86.5% of the intended design mass flow rate. The slight difference against the intended mass flow rate appears since we did not account for any blocking effect of rotor blade while designing it using the current mean-line code [\[1\]](#). A total pressure ratio Π_{TT} of 6.12 is reached at a slightly higher rotational speed of $\Omega/\Omega_o = 1.035$ for an efficiency of 75.5%.

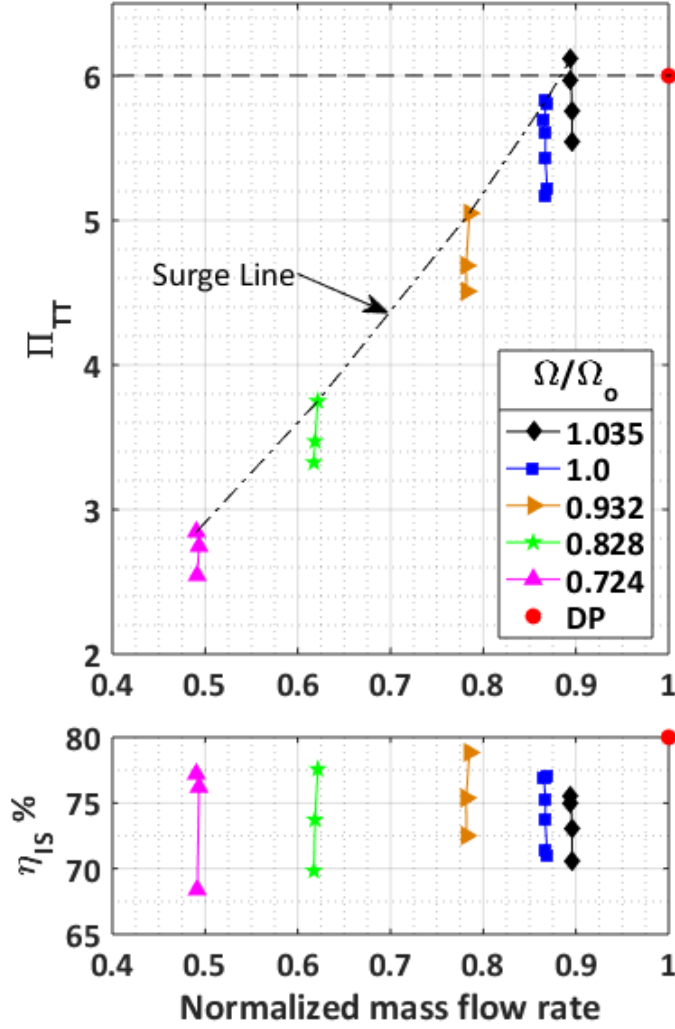


Figure 21 Stage total pressure ratio and efficiency versus normalized mass flow rate, $\Omega_0 = 28500$ RPM

The Π_{TT} and η_{IS} curves almost have a constant mass flow rate depicting choking like condition throughout their range at any Ω . This is related to the presence of shock in stator passage. As total pressure ratio of the stage increases with back pressure for the design speed as seen in Figure 22, that increment in static pressure is not sensed upstream of the stator passage shock. This effect is clearly visible as rotor performance is constant for all of the back-pressure cases explaining the constant mass flow rate. The static pressure rise pattern for different P_{03}/P_{01} cases shows that it is same up to the passage shock location in stator. Flow acceleration on SS and PS in the stator for low back pressure scenarios push shock downstream in the passage. This increases the total pressure loss due to stronger nature of passage shock reducing the stage total pressure ratio as seen in P_{03}/P_{01} curves. Contrastingly, at the maximum back pressure condition, passage shock in stator blade row '1' is located near pressure side leading-edge. Any further increment will

make the simulation unstable. Same behavior is observed in all the cases above 80% of design speed when there is presence of passage shock in stator. At a lower Ω , the performance curve varies over a range of mass flow rate values when the back-pressure increment travels upstream into rotor.

The Mach number variation obtained by local speed of sound across the stage is measured on sections perpendicular to the axis as shown in [Figure 23](#). A slight increase in the radial component is observed due to HLV stagnation zone within a subsonic regime. Work induced by the mixed flow rotor into fluid is seen as radial and tangential velocity increase. Axial component has a dip in magnitude in the $X=50$ to 100 (mm) range due to the low momentum zone generated by casing boundary layer separation. An absolute Mach number close to 1.3 as desired from the preliminary mean-line design study occurs at rotor exit. Across the vane-less space, magnitude of the radial component nearly reduces to 0 due to hub and casing contouring. This makes the stator inlet flow almost two-dimensional in nature. A sudden reduction in velocity magnitude is observed due to the passage shock. After shock, blade row '2' turns the flow resulting in reduction of the tangential component. Despite blade '2' exit angle's alignment in the axial direction, due to flow separation on SS of blade '2', a tangential velocity component still exists.

The computational "mixing plane" in between stator and rotor fluid domains to transfer circumferentially averaged quantities attributes to a slight increment in P_o and P quantities. This artificial increment corresponds to $\Pi_{TT} \sim 0.1$ as seen in [Figure 22](#). It is also seen as a sudden decrement in velocity magnitude (i.e. V_a) in [Figure 23](#). Thus, it is suggested not to consider the computational solution immediately upstream and downstream of the mixing plane for absolute flow evaluation in transonic cases [\[10\]](#).

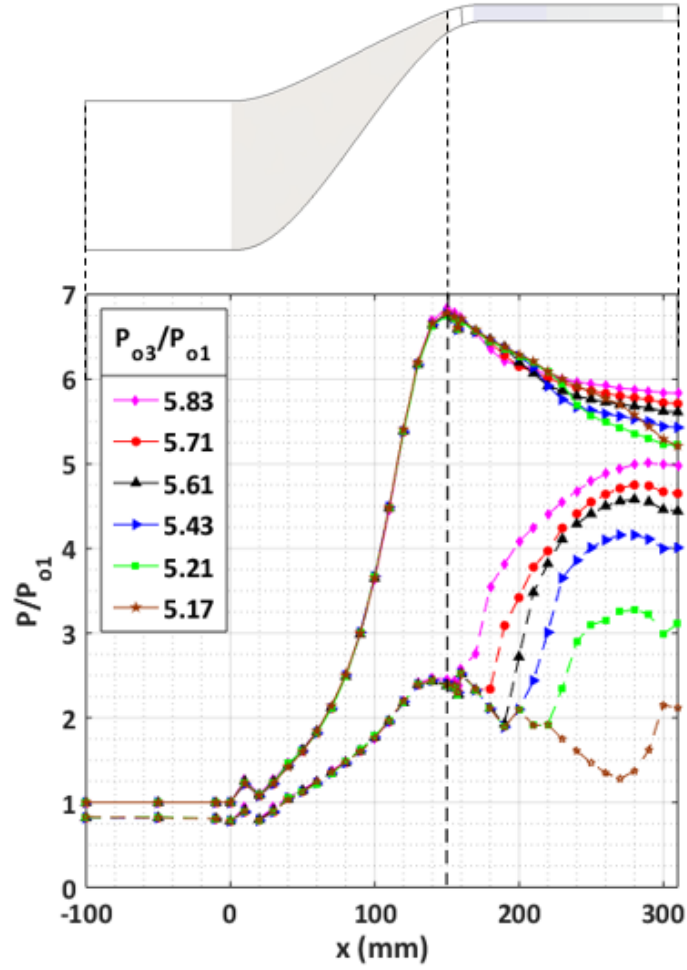


Figure 22 Stagnation pressure and static pressure distribution across the stage for different back pressures at design speed, $\Omega/\Omega_0=1.0$.

The specified design point and CFD results for the stage are compared in [Table 9](#). The CFD data is based on mass-averaged quantities. The discrepancy in \dot{m} is due to inconsideration of rotor blade blocking effect. This decrement in \dot{m} is manifested as M_1 decrement. M_2 at 1.29 is close to the desired value of 1.3. M_3 depends on the supersonic diffusion in vaneless space which is not attained as desired in this design. Flow separation on the SS of B2 accelerates the subsonic flow leading to a higher M_4 value than desired. Rotor efficiency is closer to the desired 85%.

The stage total pressure ratio at design point could be improved by increasing r_{2m} and designing a more efficient 3D diffusion system in the stator.

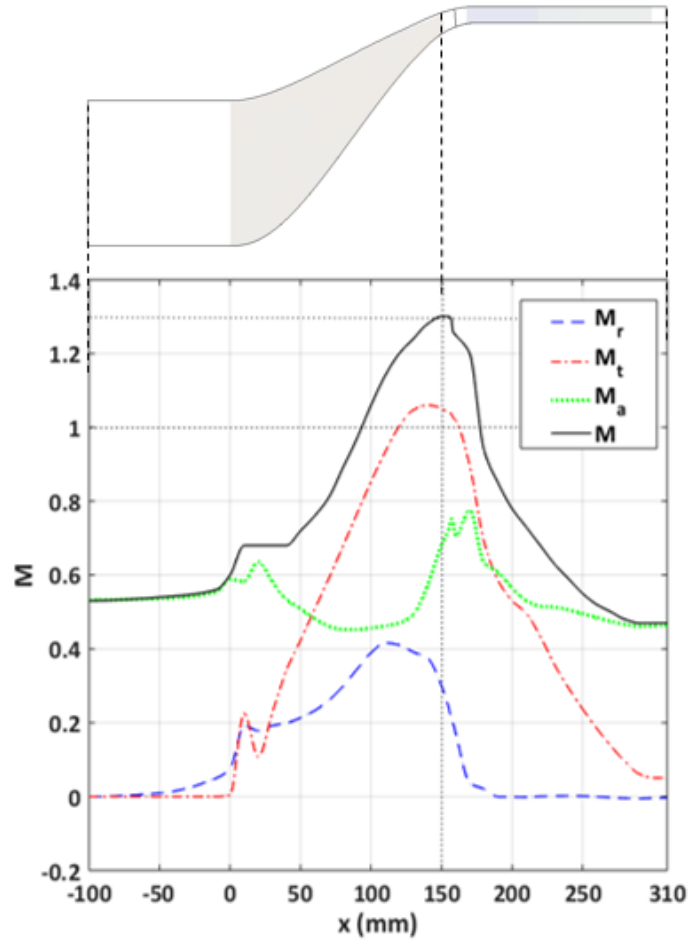


Figure 23 Velocity component distribution across the stage at design speed, $\Omega/\Omega_0=1.0$.

Table 9 Design point vs CFD comparison at maximum back pressure for the mixed-flow compressor stage

Property	Design point	CFD ($\Omega/\Omega_0=1.0$)	CFD ($\Omega/\Omega_0=1.035$)
\dot{m} (kg/s)	3.5	3.037	3.132
M_1	0.7	0.5326	0.558
M_2	1.3	1.29	1.347
M_3	1.2	1.25	1.31
M_4	0.4	0.468	0.453
Π_{TT}	6	5.83	6.12
η_{IS} (%)	75.5	76.93	75.55
η_R (%)	85	84.41	82.85
π_R	6.7	6.643	6.98

VIII. Conclusions and suggested future work

The computational viscous flow features and performance of a 6:1 total pressure ratio compressor with 75.5% efficiency designed by the in-house design code [1] has been elaborately explained in this paper. A new tandem-design supersonic diffuser [5] has been described. This new design performs better than the previous supersonic diffusion configurations by a margin of 20% in terms of efficiency. This is the key component which enables this design to achieve a very high-pressure ratio.

In order to qualify the current stage performance predictions, NASA Rotor 37 and RWTH Aachen Supersonic diffuser computations were benchmarked against experimental data to showcase the improved CFD prediction capabilities. The present computational verification effort for the CFD system used in this study resulted in stage exit total pressure and temperature predictions that are better or very similar to most of the past Rotor 37 computations. It is current authors' observation that the present computational approach can be effectively utilized in the prediction of transonic/supersonic compressor rotor flow fields in the development of better mixed-flow compressors.

The current computational method's ability to resolve the aerothermal characteristics of a supersonic diffuser with shock wave systems in it was assessed using experimental data from RWTH. This assessment was particularly important because the over-simplified mean-line system used in our design-oriented paper [1] was not able to take compressible flow effects, shock waves, three dimensionality and other viscous effects including turbulence into account. The current computations predict an isentropic efficiency of this supersonic diffuser as 72.09 %.

All except the coarse type mesh for the present mixed-flow compressor had prismatic cells sufficient enough to maintain a $Y^+ < 1$ at all grid points adjacent to the wall. Although the coarse mesh proved to be a great tool for iterating designs quickly, the rotor passage shock observed in the coarse mesh type is wider as its spread over relatively larger cells. Based on the current mesh dependency study, the moderate mesh was extensively used since it generated a stage performance that was very close to fine mesh results.

Rotor casing boundary layer separation occurring due to shock instability turns out to be the most severe loss creating mechanism. A shock stability analysis has been presented to further validate this claim. Increased hub loading makes impeller achieve higher efficiency with lower tip leakage loss and uniform flow outlet at exit. Increased tip loading makes the impeller achieve a higher-pressure ratio. The new stator design performs better than the previous supersonic diffuser attempts.

Total pressure ratio chart of this supersonic compressor has constant mass flow rate curve depicting a choking like condition. At $\Omega > 80\%$, any increment in back pressure shifts the shock location upstream in the stator but the effect does not travel upstream into the rotor. Mach number distribution across the stage shows that stator inlet flow is two dimensional in nature.

As a result of our observations from the current computational effort, following modifications are suggested for possible improvements of the stage performance. Rotor airfoil design could be improved to maintain stable shock positioning throughout the rotor passage. This unstable shock causes casing boundary layer separation which affects the rotor efficiency. Rotor leading-edge in the 0-30% span needs to be twisted to suppress leading-edge rotating spike flow feature. Hub surface near the rotor leading-edge featuring a trough would improve the loss due to HLV [25]. If 'Cs' separation is controlled η_{IS} will increase and Π_{TT} will drop due to reduction in passage diffusion.

Splitter rotor blade benefits have to be analyzed to reduce the rotor weight. Meridional contours in the vane-less space have to be optimized to enhance supersonic 3D diffusion without a normal shock. Stator airfoils, hub and casing contours may also benefit from further optimization. These changes would aid in improving the stage performance and operational range. Finally, computational simulations conclude that this mixed-flow stage design is capable of generating a total pressure ratio of 5.83 at 77.0 % efficiency at 3.03 Kg/s. A total pressure ratio Π_{TT} of 6.12 is reached at a slightly higher rotational speed of $\Omega/\Omega_o = 1.035$ for an efficiency of 75.5%.

The mean-line design procedure described in Sadagopan and Camci [1] is an effective mixed-flow compressor design system leading towards designing a high-pressure ratio mixed-flow compressor stage for aero-propulsion purposes. However, it obviously lacked to fully represent the three-dimensionality, viscous flow and compressible flow effects due to its inherent over-simplifying assumptions. The inclusion of the RANS based computations as described in this paper improved the fidelity of the mixed-flow compressor design performance calculations at a great rate.

Conflict of interest statement

The authors certify that they have NO affiliations with or involvement in any organization or entity with any financial interest (such as honoraria; educational grants; participation in speakers' bureaus; membership, employment, consultancies, stock ownership, or other equity interest; and expert testimony or patent-licensing arrangements), or non-financial interest (such as personal or professional relationships, affiliations, knowledge or beliefs) in the subject matter or materials discussed in this manuscript.

Acknowledgments

The authors wish to thank the Dept. of Aerospace Engineering for the assistantship provided to Mr. Aravinth Sadagopan. Kirk Heller and Marc Catalano's support was invaluable for maintaining the high-performance computing infrastructure for the current computations. Mitansh Doshi, Amrat Ranka, Veerandara Chakkravarthy and Gohar Khokar are thanked for providing their constructive criticism.

IX. References

- [1] Sadagopan, A., Camci, C., 2018, 'A design strategy for a 6:1 supersonic mixed-flow compressor stage', Aerospace Science and Technology, Elsevier, AESCTE 2087, *under review*.
- [2] Elmendorf, W., Kurz, H., Gallus, H.E., 1995, "Design and experimental investigation of a mixed-flow supersonic compressor stage", Presented at the International Gas Turbine and Aero-Engine Congress and Exposition, Houston, TX, June 5-8, 1995, 95-GT-379. <https://doi.org/10.1115/95-GT-379>.
- [3] Eisenlohr, G. and Benfer, F.W., 1993, "Aerodynamic design and investigation of a mixed-flow compressor stage", Presented at AGARD meeting "Technology requirements for small gas turbines", October 1993, 20-1.
- [4] Giri, G., Nassar, A., Moroz, L., Klimov, I.V., Sherbina, A., 2016, "Design and analysis of a high-pressure ratio mixed-flow compressor stage", AIAA Propulsion and Energy Forum, July 25-27, 2016, Salt Lake City, UT, AIAA 2016-4744. <https://doi.org/10.2514/6.2016-4744>
- [5] Quishi, L., Hong, W., Sheng, Z., 2009, "Application of tandem cascade for fan stator with supersonic inflow", Chinese Journal of Aeronautics 23(2010) 9-14. DOI: [10.1016/S1000-9361\(09\)60181-3](https://doi.org/10.1016/S1000-9361(09)60181-3)
- [6] Riegler, C., and Bichlmaier, C., "The geared turbofan technology-opportunities, challenges and readiness status," 1st CEAS, European Air and Space Conference, Berlin, Sep. 2007.
- [7] Kim, H.D., 2010, "Distributed propulsion vehicles", 27th Congress of the International Council of the Aeronautical Sciences 2010, ICAS 2010. 1. 55-65.
- [8] Suder, K. L., 1996, "Experimental investigation of the flow field in a transonic, axial flow compressor with respect to the development of blockage and loss", NASA TM 107310, NAS 1.15:107310, E-104
- [9] Spalart, P. R. and Allmaras, S. R., 1992, "A one-equation turbulence model for aerodynamic flows" AIAA Paper 92-0439. <https://arc.aiaa.org/doi/10.2514/6.1992-439>
- [10] STAR CCM+ 12.02.011-R8 User Manual. <http://www.cd-adapco.com/products/star-ccm/documentation>

- [11] Denton, J. D., 2010, "Some limitations of turbomachinery CFD", Proc. of ASME Turbo Expo 2010: Power for land, sea and air, June 14-18, 2010, Glasgow, UK, GT2010-22540. <https://doi.org/10.1115/GT2010-22540>.
- [12] Reid, Lonnie and Moore, Royce, D., 1978, "Performance of single-stage axial-flow transonic compressor with rotor and stator aspect ratios of 1.19 and 1.26, respectively, and with design pressure ratio of 1.82," NASA Technical Paper 1338, November 1978.
- [13] Dunham, J., 1998, "CFD Validation for propulsion system components", NATO AGARF-AR-355.
- [14] Hah, C., 2009, "Large eddy simulation of transonic flow field in NASA Rotor 37", 47th AIAA Aerospace Sciences Meeting Including the New Horizons Forum and Aerospace Exposition, Jan. 5-8, 2009, Orlando, FL. <https://arc.aiaa.org/doi/abs/10.2514/6.2009-1061>
- [15] Ameri, A., 2010, "NASA Rotor 37 CFD Code Validation (Glenn-HT Code)", NASA/CR – 2010-216235.
- [16] Boretti, A., "Experimental and computational analysis of transonic compressor rotor", 17th Australian Fluid Mechanics Conference, Auckland, New Zealand, Dec 5-9, 2010.
- [17] Bruna, D., Turner, M. G., 2013, "Isothermal boundary condition at casing applied to the Rotor 37 transonic axial flow compressor", ASME J Turbo. May 2013, Vol. 135/0.34501-1. <https://doi.org/10.1115/1.4007569>
- [18] Joo, J., Medic, G., Philips, D. A., Bose, S. T., 2014, "Large-Eddy simulation of a compressor rotor", Centre for Turbulence Research, Proceedings of the Summer Program 2014.
- [19] Seshadri, P., Parks, G. T., Shahpar, S., 2015, "Leakage uncertainties in compressors: The case of Rotor 37", AIAA Journal of Propulsion and Power, Vol. 31, No. 1, Jan-Feb 2015. <https://arc.aiaa.org/doi/10.2514/1.B35039>
- [20] Shabbir, A., Celestina, M. L., Adamczyk, J. J., Strazisar, A. J., 1997, "The effect of hub leakage flow on the two high speed axial flow compressor rotors", ASME International Gas Turbine and Aero-Engine Congress and Exhibition, Orlando, Florida – June 2-5, 1997. <https://doi.org/10.1115/97-GT-346>.
- [21] Denton, J. D., 1996, "Lessons learnt from Rotor 37", J. of Thermal Sciences, Vol. 6, No. 1. <https://doi.org/10.1007/s11630-997-0010-9>.
- [22] Monig, R., Broichhausen, K.D., Gallus, H.E., 1987, "Application of highly loaded single stage mixed flow compressors in small jet-engines", AGARD-CP-421, Paris, France, May 4-8, 1987.
- [23] Pullan, G., Young, A. M., Day, I. J., Greitzer, E. M., Spakovszky, Z. S., 2015, "Origins and structure of spike-type rotating Stall", ASME J. Turbo, May 2015, Vol. 137/051007-1. <https://doi.org/10.1115/1.4028494>.

- [24] Xuanyu, C., Xiangwei, M., Xingmin, G. and Donghai, J., 2014, "The aerodynamic design and investigation of loading distribution of a mixed-flow compressor", APISAT2014, Procedia Engineering 99(2015) 484-490. <https://doi.org/10.1016/j.proeng.2014.12.562>
- [25] Broichhausen, K. D., Ziegler, K. U., 2005, "Supersonic and transonic compressors: past, status and technology trends", Proc. of ASME Turbo Expo 2005: Power for land, sea and air, June 6-9, 2005, Reno-Tahoe, Nevada, USA, GT2005-69067. <https://doi.org/10.1115/GT2005-69067>.